FRONTIERS OF PHYSICS

RESEARCH ARTICLE
Volume 19 / Issue 6 / 63201 / 2024

Strain-engineered rippling at the bilayer-MoS_2 interface identified by advanced atomic force microscopy

Haoyu Dong[1,2,*], Songyang Li[1,2,*], Shuo Mi[1,2], Jianfeng Guo[1,2], Zhaxi Suonan[1,2], Hanxiang Wu[1,2], Yanyan Geng[1,2], Manyu Wang[1,2], Huiwen Xu[1,2], Li Guan[3], Fei Pang[1,2], Wei Ji[1,2], Rui Xu[1,2,†], Zhihai Cheng[1,2,‡]

1 Beijing Key Laboratory of Optoelectronic Functional Materials & Micro-Nano Devices, Department of Physics, Renmin University of China, Beijing 100872, China
2 Key Laboratory of Quantum State Construction and Manipulation (Ministry of Education), Renmin University of China, Beijing 100872, China
3 Key Laboratory of Advanced Light Conversion Materials and Biophotonics, Department of Chemistry, Renmin University of China, Beijing 100872, China
*These authors contributed equally to this work.
Corresponding authors. E-mail: †ruixu@ruc.edu.cn, ‡zhihaicheng@ruc.edu.cn
Received March 11, 2024; accepted April 13, 2024

ABSTRACT

The van der Waals interface structures and behaviors are of great importance in determining the physical properties of two-dimensional atomic crystals and their heterostructures. The delicate interfacial properties are sensitively dependent on the mechanical behaviors of atomically thin films under external strain. Here, we investigated the strain-engineered rippling structures at the CVD-grown bilayer-MoS_2 interface with advanced atomic force microscopy (AFM). The in-plane compressive strain is sequentially introduced into the 1L-substrate and 2L-1L interface of bilayer-MoS_2 flakes via a fast-cooling process. The thermal strain-engineered rippling structures were directly visualized at the central 2H- and 3R-MoS_2 bilayer regions with friction force microscopy (FFM) and bimodal AFM techniques. These rippling structures can be further artificially manipulated into the beating-like rippling features and fully erased via the contact mode AFM scanning. Our results shed lights on the strain-engineered interfacial structures of two-dimensional materials and also inspire the further investigation on the interface engineering of their electronic and optical properties.

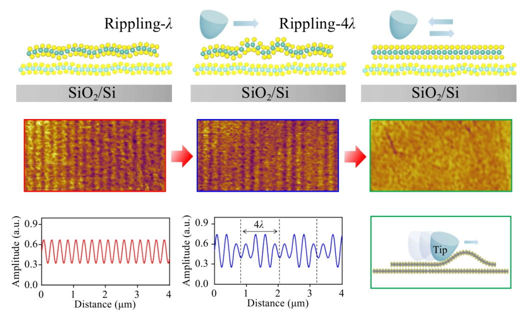

Keywords rippling, interface, strain-engineered, atomic force microscopy, transition metal dichalcogenides

1 Introduction

Two-dimensional (2D) semiconducting layered transition metal dichalcogenides (TMDs), such as MoS_2 and WS_2, have attracted great attention owing to their bandgap crossover from direct in the monolayer to indirect in the bilayer and bulk, showing a wide range of potential applications in optoelectronic and photonic devices [1–10]. Chemical vapor deposition (CVD) has been developed to synthesize low-cost and scalable 2D TMD monolayer and bilayer films for practical device applications [9, 11–16]. The CVD-grown TMD monolayer and/

Higher Education Press

https://doi.org/10.1007/s11467-024-1409-4

or bilayer flakes can also be further artificially stacked to fabricate 2D heterostructures with many emergent exotic quantum states [17–20]. The diversity of 2D crystals results in a large number of possible 2D heterostructures that possess interesting properties and functions for applications [21]. However, in contrast to their extensively studied electrical and optical properties, the mechanical properties and behaviors of 2D TMDs and their heterostructures have not been well characterized, especially mechanical properties of their delicate homo- and hetero-interface.

Since electronic and mechanical properties of multilayered 2D crystals critically depend on their interlayer interactions [21–23], understanding the influence of the external mechanical perturbations on the interlayer as well as intralayer interactions is very important. Strain-engineering is a powerful method to tailor the physical properties of monolayer 2D materials [24–27]. For example, several groups have pointed out theoretically that strain can modify the bandgap of 2D TMDs effectively [4, 25, 28–32]. Although many emergent properties have been discovered and reported in the multilayered 2D crystals, the strain-engineering of homo- and/or hetero-interface in these materials have been rarely discussed.

In this work, we reported the real-space investigation of the strain-engineered rippling structures at the two interfaces of bilayer-MoS_2 on the SiO_2/Si substrate with two advanced AFM techniques. The in-plane compressive strain was applied on the bilayer-MoS_2 flakes through the fast-cooling process after the CVD growth. By using the multifrequency AFM, the strain-induced three-fold symmetric ripple structures of the bottom layer were successfully visualized in the bimodal images via their specific mechanical properties. These ripple structures were affected by the central 2H- and 3R-MoS_2 bilayer regions due to their larger Young's modulus than monolayer. The approximately zigzag-orientated rippling lines were further visualized exclusively within the top-layer of 2H- and 3R-bilayer regions. These linear rippling lines can be artificially manipulated into the beating-like rippling structures and fully erased via the contact mode AFM scanning. The formation and manipulation mechanism of rippling lines was phenomenally discussed based on the strain-induced anisotropic mechanical properties and the wave-like interfacial strain at the 2L-interface.

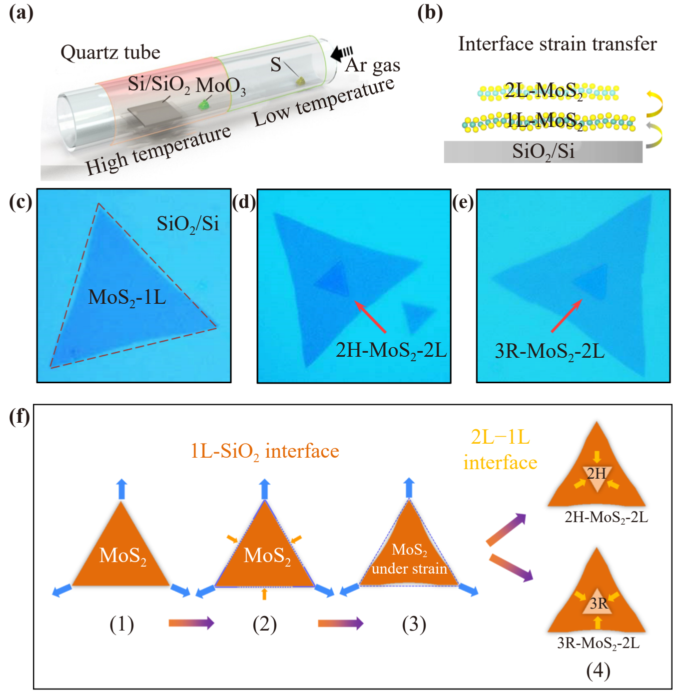

Fig. 1 Growth of triangular monolayer- and bilayer-MoS_2 flakes and the introduction of interfacial strain. **(a)** Schematic diagram for the CVD growth of MoS_2. **(b)** The in-plane isotropic compressive strain can be subsequentially applied into the bottom and top MoS_2 layer via the 1L-substatre and 2L–1L interface. **(c–e)** Optical images of the CVD-grown MoS_2 monolayer (c), 2H-MoS_2 (d) and 3R-MoS_2 (e) bilayer triangular flakes. **(f)** Schematic formation mechanism for the strain-engineered vein-like MoS_2 monolayer flake, and the 2H- and 3R-MoS_2 bilayer flakes of (c–e).

2 Results and discussion

The micro-scale triangular MoS_2 flakes were grown on the SiO_2/Si substrates by the traditional low-pressure chemical vapor deposition (LPCVD) method, as shown in Fig. 1(a). After the CVD growth, the tensive strain was induced into the bottom MoS_2 layer (1L) and the top layer (2L) via the 1L-substrate and 2L–1L interface bonding during the following fast-cooling process, which is due to the difference between the thermal expansion coefficients (TEC) of the MoS_2 flake (10^{-5} K^{-1}) and the underlying SiO_2/Si substrate (10^{-7} K^{-1}) [33, 34]. To retain the strain within the flakes generated from the TCE-mismatch, the interface and edge bonding between the 1L-MoS_2 and the underlying substrate must be sufficiently strong to maintain the non-slippery condition. As shown in Fig. 1(f), when the accumulated tensive strain is too large to be retained by the underlying substrate, the interface slip will happen and the flake will partially shrink from the edges. Then, the compressive strain will be introduced within the MoS_2 flakes during the shrinking process [35]. Considering the relative weaker interfacial 1L–2L bonding, the above tensive-compressive strain was only partially applied onto the top layer of the MoS_2 bilayer flake, resulting in a minimal strain within the 2L-MoS_2.

Figure 1(c) shows the optical image of the typical triangular MoS_2 monolayer flakes due to the above strain-engineered process, which are called vein-like flakes according to their specific geometrical shapes of partially curved edges at the middle regions [35]. Furthermore, the second MoS_2 layer can grow at the

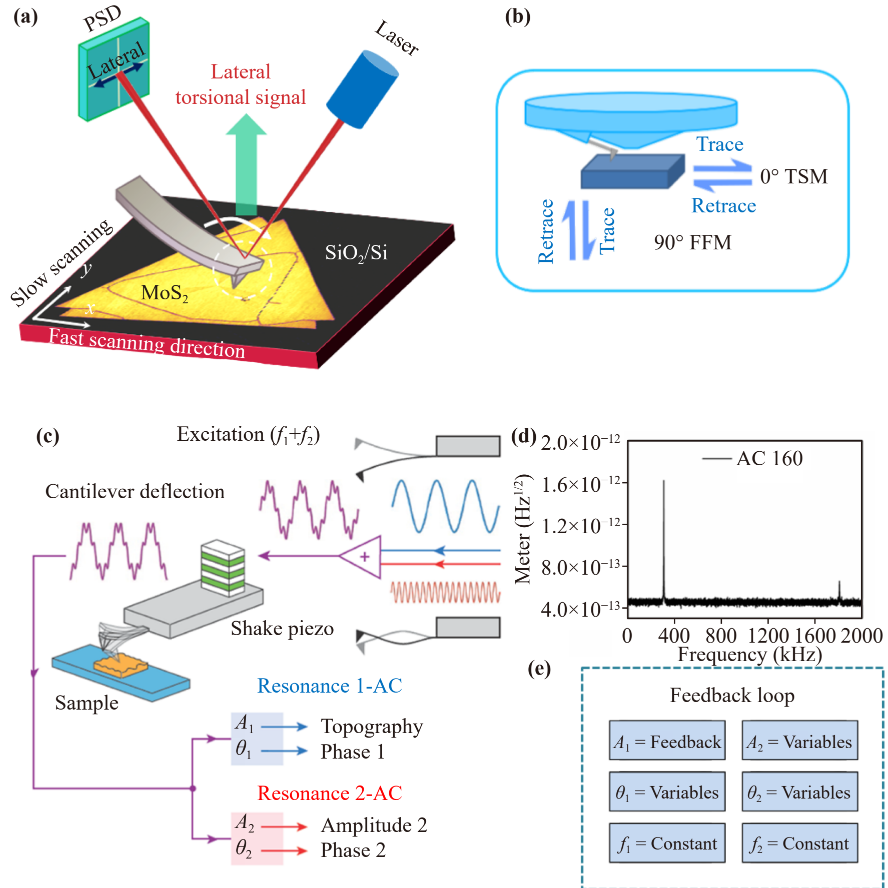

Fig. 2 Schematics of bimodal AFM and FFM. **(a)** Schematic of FFM mode. PSD, acronym for position-sensitive detector. **(b)** Scanning directions for FFM and TSM imaging. Here, the direction of scanning is perpendicular (parallel) to the cantilever axis for FFM (TSM) imaging. The FFM friction image is obtained by detecting the lateral torsional signal of PSD in FFM. **(c)** Schematic experimental setup of bimodal AFM. **(d)** Resonance frequencies of AFM probe (AC160) at the first and second eigenmode of cantilever. **(e)** Simplified scheme for the used feedback loops in bimodal AFM.

center of these triangular flakes and exhibits triangular shape in the 2H- or 3R-MoS_2 bilayer structure. The optical images of 2H- and 3R-MoS_2 bilayer polytypes are shown in Figs. 1(d) and (e), respectively. It is noted that the introduced interfacial strain within the monolayer and bilayer MoS_2 flakes during the fast-cooling process could affect the geometric shapes and strain-engineered features at the 1L-substare and 2L–1L interface, as schematically illustrated in Fig. 1(f). While no distinctive strain-engineered features were observed in the optical images of vein-like monolayer and bilayer MoS_2 flakes, the bimodal AFM and friction force microscopy (FFM) modes were further used to characterize the strain-induced nanostructures of these MoS_2 flakes.

All of the AFM measurements were carried out on a commercial AFM (MFP-3D Infinity, Asylum Research) under ambient environment. FFM is one of basic AFM operation modes, which can map friction forces between the tip and sample by measuring the lateral torsion of cantilever while contact scanning along its perpendicular direction, as shown in Figs. 2(a) and (b) [36–38]. In our previous work, the FFM mode has been successfully used to image the strain-induced hierarchical ripples in MoS_2 layers [39]. The bimodal AFM is a multifrequency mode that uses two eigenmode frequencies of AFM cantilever [40]. In this mode, the cantilever is simultaneously driven at two of its eigenmodes (resonant modes), as shown in Fig. 2(c). The first resonance mode of cantilever operates the same as regular amplitude modulation mode (i.e., tapping mode). Additionally, the second resonance mode works without any feedback and its amplitude (A_2) and phase (P_2) response are recorded. The A_2 and P_2 images of second mode can provide enhanced contrast and spatial details of the samples by qualitatively detecting their local mechanical properties (energy dissipation) of the sample. The silicon AFM probes (AC160, Asylum Research) were used in FFM and bimodal AFM mode, which typically have specific tip radius R ~ 7 nm, force constant k ~ 26 N/m, and the resonance frequency of first resonance mode f_{r1} ~ 300 kHz and second resonance mode f_{r2} ~ 1800 kHz, as shown in Fig. 2(d). The feedback loop of bimodal AFM

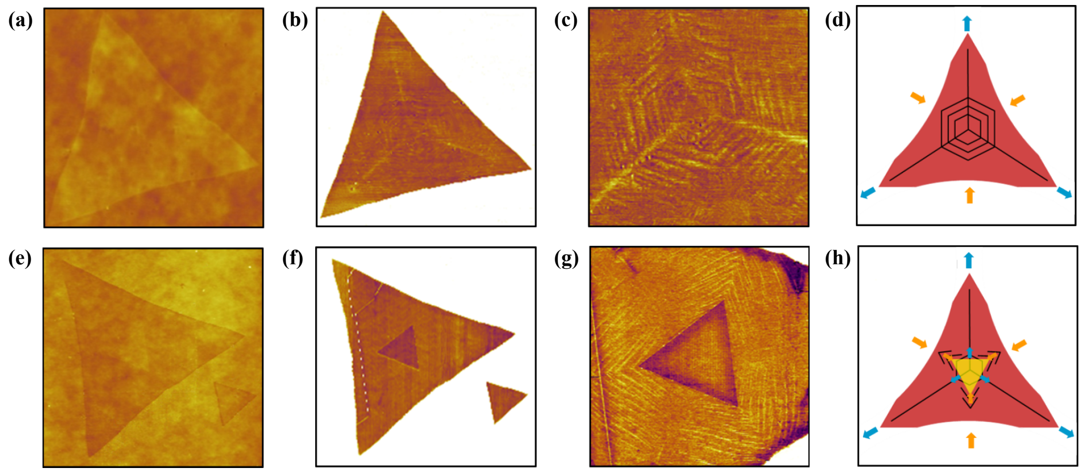

Fig. 3 Strain-engineered ripple structures of the vein-like monolayer and 2H-MoS_2 bilayer flake. **(a, b)** The AFM topography (a) and corresponding FFM friction (b) images of vein-like MoS_2 monolayer on the SiO_2/Si substrates. **(c)** The zoom-in image of (b) at the central region. **(d)** Schematic formation mechanism for the strain-engineered ripple structures in the monolayer flake. **(e, f)** The AFM topography (e) and corresponding FFM friction (f) images of 2H-MoS_2 bilayer flake on the SiO_2/Si substrates. **(g)** The zoom-in image of (f) at the central region. **(h)** Schematic formation mechanism for the strain-engineered triangular 2H-MoS_2 bilayer flake. It is noted that the central top layer of 2H-MoS_2 is under the interfacial compression via the compressive bottom layer. Image size: (a, b) 45 μm; (c) 16 μm. (e, f) 60 μm; (g) 25 μm.

mode is schematically shown in Fig. 2(e), in which the A_2 amplitude channel is used to characterize the strain-engineered features of the bilayer-MoS_2 interface.

The strain-induced structures of vein-like MoS_2 monolayer flakes were clearly observed in FFM mode. Figure 3(a) shows the AFM topography image of typical vein-like MoS_2 monolayer flake, in which no specific features are observed. The distinctive strain-induced features were clearly observed by the FFM mode, as shown in Fig. 3(b), in which three straight lines originating from the center to the corner apex were observed. The inset zoomed-in image of Fig. 3(c) clearly shows the compressive strain-induced hierarchical hexagonal ripple pattern at the central region. A simple formation mechanism was proposed based on the interface slip at the middle part of edges, as schematically shown in Fig. 3(d). Since the thermal expansion coefficient of MoS_2 is larger than that of the SiO_2/Si substrate, local tensile strain will be induced into the MoS_2 flake during the cooling process. When the size of triangular MoS_2 flakes is larger than the critical value, the edge and interface bonding could not retain the accumulated tensile strain within the flakes. Considering their triangular geometry, the interface slip will first happen at the middle edges, and the flake will partially shrink from these edges and form the vein-like nanoripple patterns.

The thickness and polytype of bilayer-MoS_2 flakes can affect their strain-engineered structures. Figure 3(e) shows the AFM topography image of 2H-MoS_2 bilayer polytype flake, in which no distinctive strain-engineered features were observed. However, the three-fold strain-induced ripple patterns around the central bilayer regions were observed, as shown in the FFM images of Figs. 3(f) and (g). It is noted that these nanoripples are located only at the first layer and shifted away from central bilayer regions of the whole flakes, in comparison with the central ripple patterns within the monolayer vein-like flakes. Their formation mechanism can be understood based on the different mechanical properties of monolayer and bilayer MoS_2. The Young's modulus of the bilayer is larger than that of monolayer. Then, the ripples formed at the monolayer areas around the central triangular bilayer region, as shown in Fig. 3(h). It is also noted that the central bilayer-MoS_2 regions are under centripetal compressive strain, while no clear strain-engineered feature is observed even in the FFM images.

It is noticed that no significant deformation is observed in the small MoS_2 flake, shown in the lower right corner of Fig. 3(f). The reason is that the magnitude of stress within the MoS_2 flakes is positively correlated with the size of the sample; the larger the sample, the greater the stress within it. For small MoS_2 flakes, the stress within it is very small and insufficient to cause deformation of the sample.

The 1L-MoS_2 were characterized by Raman and PL spectra, as shown in Fig. S1 of the Electronic Supplementary Materials (ESM), which confirmed our hypothesis about the strain distribution. However, the Raman and PL spectra of the 2L-MoS_2 are indistinguishable from the unstressed MoS_2, as the interfacial stress imparted by the 1L-MoS_2 is minimal to a negligible extent.

The strain-engineered rippling lines at the 2H-MoS_2 bilayer interface were distinctively visualized via the bimodal AFM imaging. Figures 4(a) and (b) show the AFM topography and bimodal (A_2) images of the 2H-

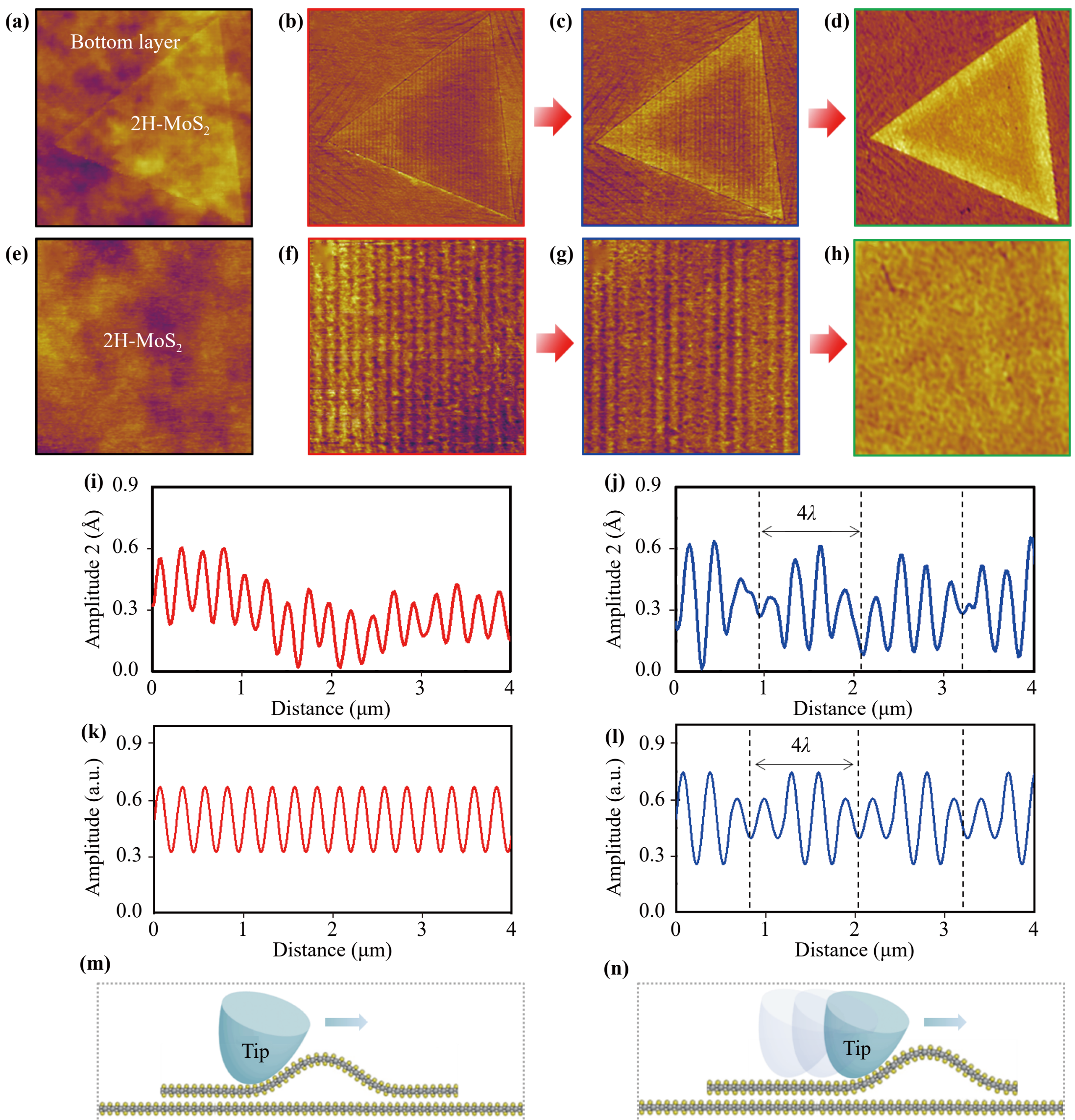

Fig. 4 Strain-engineered rippling at the 2H-MoS_2 bilayer interface. **(a)** The AFM topography images of the top layer at the central region of 2H-MoS_2 bilayer flake in Fig. 3(e). The 2H-stacked top layer is indicated by 2H-MoS_2. No strain-induced features can be observed in the topography image. **(b–d)** The bimodal AFM images (A_2) of the same area of (a) obtained before (b), during (c) and after (d) the repeated contact mode scanning. **(e–h)** The corresponding zoom-in images of (a–d) at the central area of 2H-toplayer. The strain-induced rippling features are observed within the 2H-toplayer in the bimodal AFM images and can be manipulated by contact mode AFM scanning. **(i, j)** The corresponding averaged line profiles of rippling features in (f) and (g). **(k, l)** Schematics of the uniform compressive wave for (i) and the beating-like compressive wave ($\lambda_B = 4\lambda$) for (j). **(m, n)** Schematics for the contact mode scanning (m) and erasing process (n) of the rippling. Image Sizes: (a–d) 13 μm; (e–h) 4 μm.

MoS_2 bilayer region at the center of 2H-MoS_2 flake of Fig. 3(e), respectively. No distinctive rippling features were observed in the topography image, while the linear rippling lines were clearly visualized in the bimodal AFM image. The orientation of rippling lines is not perfectly along one of three zigzag crystallographic orientations but with a small angle of ~7°. It is noted that the three-fold symmetry is broken for these rippling lines of the 2H-toplayer via the three-fold symmetric compressive strain applied by the underlying bottom MoS_2 layer. In our previous work, the similar zigzag-orientated rippling lines can also be formed in the monolayer WS_2 flake via the isotropic compressive strain applied by the underlying amorphous SiO_2/Si substrates [38]. While these rippling lines cannot be directly visualized in the AFM images, but can only be indirectly determined by the angle-dependent transverse shear microscopy (TSM).

Figures 4(e) and (f) show the zoom-in topography and bimodal (A_2) images of the linear rippling lines at the

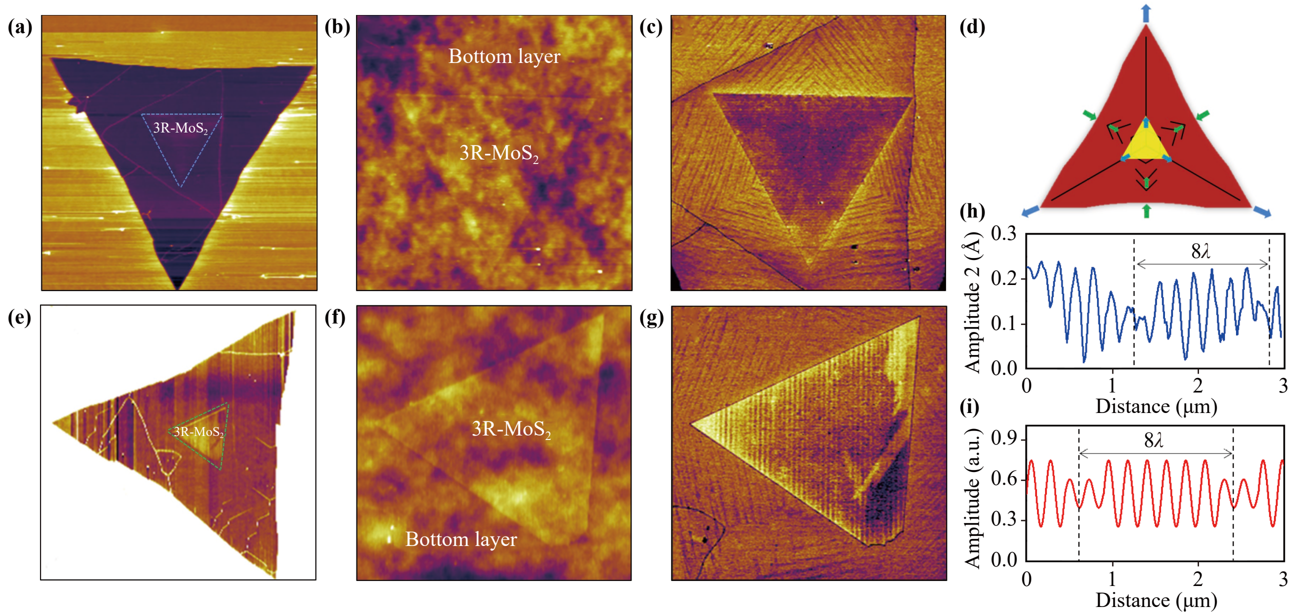

Fig. 5 Strain-engineered rippling at the 3R-MoS$_2$ bilayer interface. **(a)** The FFM friction image of the 3R-MoS$_2$ bilayer flake. The 3R-stacked top layer is indicated by 3R-MoS$_2$. **(b)** The AFM topography image of the central 3R-MoS$_2$ bilayer region in (a). **(c)** The corresponding bimodal AFM image (A$_2$) of (b). **(d)** Schematic formation mechanism for the strain-engineered triangular 3R-MoS$_2$ bilayer flake. It is noted that the central top layer of 3R-MoS$_2$ is under interfacial compression via the compressive bottom layer. **(e)** The FFM friction image of another 3R-MoS$_2$ bilayer flake. **(f)** The AFM topography image of the central 3R-MoS$_2$ bilayer region in (e). **(g)** The corresponding bimodal AFM image (A$_2$) of (f). **(h)** Averaged line profile of the rippling in (g). **(i)** Schematic of the beating-like compressive wave ($\lambda_B = 8\lambda$) for (h). Image size: (a) 58 μm; (b, c) 23 μm; (d) 50 μm; (e, f) 11 μm.

2H-MoS$_2$ bilayer interface, respectively. No morphology of rippling lines but only surface corrugation of the underlying amorphous SiO$_2$/Si substrate was observed in the topography image. This is because the height of rippling structure is smaller than the resolution limit of AFM topography images, so the rippling structure is indistinguishable in Fig. 4(e). The rippling lines were clearly resolved in the bimodal (A$_2$) image of Fig. 4(f), and was further indicated by the corresponding horizontal line profile of Fig. 4(i) with the periodicity (or wavelength) of ~236 nm. It is noted that this in-plane wavelength (~236 nm) is two orders of magnitude larger than the thickness of MoS$_2$ monolayer (~1 nm), which agrees with the invisible morphology of rippling lines in topography images. The observed rippling lines in the bimodal AFM images could be attributed to the periodical partial-delamination at the 2H-MoS$_2$ bilayer interface under the compressive strain. According to the previous work, the large (small) A$_2$ value means the stiff (soft) local mechanical property with small (larger) energy dissipation during the bimodal AFM mode imaging [41]. It is clear that the partial-delamination regions represent the local smaller stiffness due to the weaker interfacial bonding that the non-delamination regions at the 2H-MoS$_2$ bilayer interface.

The periodical partial-delamination of the 2H-MoS$_2$ interface can be further manipulated and gradually erased by the contact mode AFM scanning, as shown in Figs. 4(b–d) and (f–h). During the erasing process, the uniform linear rippling lines were manipulated into the specific beating-like rippling lines, as shown in Fig. 4(c), while the three-fold symmetric ripple patterns at the bottom layer remained unchanged. The beating-like rippling lines were clearly resolved in the bimodal (A$_2$) image of Fig. 4(g), and was further indicated by the corresponding horizontal line profile of Fig. 4(j) with the fundamental and beating wavelengths of ~294 nm and ~1178 nm, respectively. Figures 4(k) and (l) show the ideal schematics of the observed uniform and beating-like compressive waves at a ratio of 1/4 for the observed rippling line features at the 2H-bilayer interface. The rippling lines can be completely nonreversible erased by further AFM scanning, as shown in Figs. 4(d) and (h), which can be schematically illustrated by the cartoons of Figs. 4(m) and (n).

The strain-engineered rippling lines were also visualized at the 3R-MoS$_2$ bilayer flakes, as shown in Fig. 5. Figure 5(a) shows the FFM image of one typical 3R-MoS$_2$ bilayer flake. The corresponding AFM topography and bimodal (A$_2$) images of the 3R-bilayer region at the center of 3R-MoS$_2$ flake are shown in Figs. 5(b) and (c), respectively. The strain-induced three-fold ripple patterns in the underlaying layer around the central 3R-bilayer were clearly resolved in the bimodal AFM image.

Their formation mechanism is very similar to those within the 2H-MoS_2 flake, as schematically shown in Fig. 5(d). The rippling structure in 2H- and 3R-MoS_2 exhibited slight difference attributed to the distinct stacking configurations and properties such as interlayer bonding between 1L- and 2L-MoS_2. It is also noted that the linear rippling lines can be only vaguely resolved within the 3R-top layer region in Fig. 5(c). Figure 5(e) shows the FFM image of another typical 3R-MoS_2 bilayer flake. The corresponding AFM topography and bimodal (A_2) images of the 3R-bilayer region at the center of 3R-MoS_2 flake are shown in Figs. 5(f) and (g), respectively. The beating-like rippling lines were also observed at the 3R-MoS_2 bilayer flake of Fig. 5(g). Figure 5(h) shows the corresponding horizontal line profile of the beating-like rippling features in Fig. 5(g), and schematically illustrated by Fig. 5(i) with the 1/8 ratio of fundamental and beating wavelength at the 3R-bilayer interface. The bilayer MoS_2 on the SiO_2/Si can be simplified to the film/substrate bilayer system (Fig. S2 of the ESM). These rippling structures induced by the repeated scanning are phenomenally similar to the period-doubling feature in mechanics (Fig. S3 of the ESM), which can be phenomenally described by beating-like feature (Fig. S4 of the ESM).

Considering the large size and complexity of the observed structures, the formation and manipulation mechanism of these strain-engineered rippling features at the 2L-MoS_2 interface can only be phenomenally discussed here. Firstly, the underlying substate can introduced tensive-compressive strain into the bottom MoS_2 layer via the strong MoS_2–SiO_2 interface, and subsequentially into the top MoS_2 layer via the weak MoS_2–MoS_2 interface during the fast-cooling process. Secondly, the observed linear uniform rippling can be assumed as one-dimensional stress waves with periodical interfacial adhesion and declamations. Due to their two-dimensional nature, the out-of-plane deformation height is only a tiny portion of the intrinsic interfacial distance, which cannot be visualized by the normal AFM topography imaging. By detecting their different mechanical properties, the wave-like rippling was spatially detected by bimodal AFM and FFM. It is also noted that the rippling line is approximately parallel to one of the zigzag directions, which is attributed to the large (small) stiffness of zigzag (armchair) crystallographic orientations for the MoS_2 layer. Finally, via contact AFM scanning process, the pristine uniform rippling can be manipulated into the beating-like rippling lines by partially releasing the compressive strain-energy. While the detailed underlying mechanism for these interesting beating-like rippling is still an open question worthy of further study in future.

3 Conclusions

In summary, we have systematically investigated the strain-engineered rippling structures at the interface of bilayer-MoS_2 with FFM and bimodal AFM techniques. The in-plane tensive and compressive strain was applied on the bilayer-MoS_2 flakes through the fast-cooling process after the high-temperature CVD growth. The strain-engineered rippling structures were directly visualized at the central 2H- and 3R-MoS_2 bilayer regions, indicating the compression-induced interfacial linear wave-like delamination. These uniform rippling lines can be artificially manipulated into the beating-like rippling structures and fully erased via the contact mode AFM scanning. The formation and manipulation mechanism of rippling lines was phenomenally discussed based on the strain-induced anisotropic mechanical properties and the wave-like interfacial strain distribution. It is intriguing to conduct transport measurements of the rippling structures, while we found it is hard to maintain the rippling structure during transport measurement. The transport measurement of the rippling structure requires more advanced techniques, which needs further investigation in future research. We believe that this periodical rippling structure can be used as a two-dimensional electronic superlattice in a broad range of electronic and optoelectronic devices. These results will not only shed lights on the strain-induced interfacial structures but also inspire the further investigation on the interfacial-engineered electronic and optical properties of two-dimensional materials, especially for the CVD-grown heterostructures.

Declarations The authors declare that they have no competing interests and there are no conflicts.

Electronic supplementary materials The online version contains supplementary material available at https://doi.org/10.1007/s11467-024-1409-4 and https://journal.hep.com.cn/fop/EN/10.1007/s11467-024-1409-4.

Acknowledgements This project was supported by the National Key R&D Program of China (MOST) (Grant Nos. 2023YFA1406500 and 2018YFE0202700), the National Natural Science Foundation of China (NSFC) (Nos. 21622304, 61674045, 11604063, 11974422, and 12104504), the Strategic Priority Research Program (Chinese Academy of Sciences, CAS) (No. XDB30000000), and the Fundamental Research Funds for the Central Universities and the Research Funds of Renmin University of China [Nos. 21XNLG27 (Z.C.) and 22XNH095 (H.D.)]. Y. Y. Geng was supported by the Outstanding Innovative Talents Cultivation Funded Programs 2023 of Renmin University of China.

References

1. H. T. Yuan, H. T. Wang, and Y. Cui, Two-dimensional layered chalcogenides: From rational synthesis to property control via orbital occupation and electron filling, *Acc. Chem. Res.* 48(1), 81 (2015)
2. S. Hussain, K. Q. Xu, S. L. Ye, L. Lei, X. M. Liu, R.

Xu, L. M. Xie, and Z. H. Cheng, Local electrical characterization of two-dimensional materials with functional atomic force microscopy, *Front. Phys.* 14(3), 33401 (2019)

3. Z. Lin, A. McCreary, N. Briggs, S. Subramanian, K. H. Zhang, Y. F. Sun, X. F. Li, N. J. Borys, H. T. Yuan, S. K. Fullerton-Shirey, A. Chernikov, H. Zhao, S. McDonnell, A. M. Lindenberg, K. Xiao, B. J. LeRoy, M. Drndic, J. C. M. Hwang, J. Park, M. Chhowalla, R. E. Schaak, A. Javey, M. C. Hersam, J. Robinson, and M. Terrones, 2D materials advances: From large scale synthesis and controlled heterostructures to improved characterization techniques, defects and applications, *2D Mater.* 3(4), 042001 (2017)
4. G. Plechinger, A. Castellanos-Gomez, M. Buscema, H. S. J. van der Zant, G. A. Steele, A. Kuc, T. Heine, C. Schuller, and T. Korn, Control of biaxial strain in single-layer molybdenite using local thermal expansion of the substrate, *2D Mater.* 2(1), 015006 (2015)
5. S. Bertolazzi, J. Brivio, and A. Kis, Stretching and breaking of ultrathin MoS_2, *ACS Nano* 5(12), 9703 (2011)
6. P. Johari and V. B. Shenoy, Tuning the electronic properties of semiconducting transition metal dichalcogenides by applying mechanical strains, *ACS Nano* 6(6), 5449 (2012)
7. A. McCreary, R. Ghosh, M. Amani, J. Wang, K. A. N. Duerloo, A. Sharma, K. Jarvis, E. J. Reed, A. M. Dongare, S. K. Banerjee, M. Terrones, R. R. Namburu, and M. Dubey, Effects of uniaxial and biaxial strain on few-layered terrace structures of MoS_2 grown by vapor transport, *ACS Nano* 10(3), 3186 (2016)
8. J. W. Wang, L. Q. He, Y. H. Zhang, H. Y. Nong, S. N. Li, Q. K. Wu, J. Y. Tan, and B. L. Liu, Locally strained 2D materials: Preparation, properties, and applications, *Adv. Mater.* 2024, 2314145 (2024)
9. R. Xu, Y. Lun, L. Meng, F. Pang, Y. Pan, Z. Zheng, L. Lei, S. Hussain, Y. J. Li, Y. Sugawara, J. Hong, W. Ji, and Z. Cheng, Visualization of strain-engineered nanopattern in center-confined mesoscopic WS_2 monolayer flakes, *J. Phys. Chem. C* 126(16), 7184 (2022)
10. L. Lei, J. Q. Dai, H. Y. Dong, Y. Y. Geng, F. Y. Cao, C. Wang, R. Xu, F. Pang, Z. X. Liu, F. S. Li, Z. H. Cheng, G. Wang, and W. Ji, Electronic Janus lattice and kagome-like bands in coloring-triangular $MoTe_2$ monolayers, *Nat. Commun.* 14(1), 6320 (2023)
11. K. K. Liu, W. J. Zhang, Y. H. Lee, Y. C. Lin, M. T. Chang, C. Su, C. S. Chang, H. Li, Y. M. Shi, H. Zhang, C. S. Lai, and L. J. Li, Growth of large-area and highly crystalline MoS_2 thin layers on insulating substrates, *Nano Lett.* 12(3), 1538 (2012)
12. B. L. Liu, M. Fathi, L. Chen, A. Abbas, Y. Q. Ma, and C. W. Zhou, Chemical vapor deposition growth of monolayer WSe_2 with tunable device characteristics and growth mechanism study, *ACS Nano* 9(6), 6119 (2015)
13. Y. H. Lee, X. Q. Zhang, W. J. Zhang, M. T. Chang, C. T. Lin, K. D. Chang, Y. C. Yu, J. T. W. Wang, C. S. Chang, L. J. Li, and T. W. Lin, Synthesis of large-area MoS_2 atomic layers with chemical vapor deposition, *Adv. Mater.* 24(17), 2320 (2012)
14. H. Zeng, Y. Wen, L. Yin, R. Q. Cheng, H. Wang, C. S. Liu, and J. He, Recent developments in CVD growth and applications of 2D transition metal dichalcogenides, *Front. Phys.* 18(5), 53603 (2023)
15. R. Xu, F. Pang, Y. H. Pan, Y. Z. Lun, L. Meng, Z. Y. Zheng, K. Q. Xu, L. Lei, S. Hussain, Y. J. Li, Y. Sugawara, J. W. Hong, W. Ji, and Z. H. Cheng, Atomically asymmetric inversion scales up to mesoscopic single-crystal monolayer flakes, *ACS Nano* 14(10), 13834 (2020)
16. R. Xu, S. L. Ye, K. Q. Xu, L. Lei, S. Hussain, Z. Y. Zheng, F. Pang, S. Y. Xing, X. M. Liu, W. Ji, and Z. H. Cheng, Nanoscale charge transfer and diffusion at the MoS_2/SiO_2 interface by atomic force microscopy: Contact injection versus triboelectrification, *Nanotechnology* 29(35), 355701 (2018)
17. K. Chen, X. Wan, J. X. Wen, W. G. Xie, Z. W. Kang, X. L. Zeng, H. J. Chen, and J. B. Xu, Electronic properties of MoS_2-WS_2 heterostructures synthesized with two-step lateral epitaxial strategy, *ACS Nano* 9(10), 9868 (2015)
18. L. Britnell, R. M. Ribeiro, A. Eckmann, R. Jalil, B. D. Belle, A. Mishchenko, Y. J. Kim, R. V. Gorbachev, T. Georgiou, S. V. Morozov, A. N. Grigorenko, A. K. Geim, C. Casiraghi, A. H. C. Neto, and K. S. Novoselov, Strong light-matter interactions in heterostructures of atomically thin films, *Science* 340(6138), 1311 (2013)
19. B. Hunt, J. D. Sanchez-Yamagishi, A. F. Young, M. Yankowitz, B. J. LeRoy, K. Watanabe, T. Taniguchi, P. Moon, M. Koshino, P. Jarillo-Herrero, and R. C. Ashoori, Massive dirac fermions and hofstadter butterfly in a van der Waals heterostructure, *Science* 340(6139), 1427 (2013)
20. K. S. Novoselov, A. Mishchenko, A. Carvalho, and A. H. Castro Neto, 2D materials and van der Waals heterostructures, *Science* 353(6298), aac9439 (2016)
21. R. Xu, X. S. Wang, Z. Y. Zheng, S. L. Ye, K. Q. Xu, L. Lei, S. Hussain, F. Pang, X. M. Liu, Y. J. Li, Y. Sugawara, W. Ji, L. M. Xie, and Z. H. Cheng, Interfacial water intercalation-induced metal–insulator transition in NbS_2/BN heterostructure, *Nanotechnology* 30(20), 205702 (2019)
22. A. F. Rigosi, H. M. Hill, Y. Li, A. Chernikov, and T. F. Heinz, Probing interlayer interactions in transition metal dichalcogenide heterostructures by optical spectroscopy: MoS_2/WS_2 and $MoSe_2/WSe_2$, *Nano Lett.* 15(8), 5033 (2015)
23. K. Liu, Q. M. Yan, M. Chen, W. Fan, Y. H. Sun, J. Suh, D. Y. Fu, S. Lee, J. Zhou, S. Tongay, J. Ji, J. B. Neaton, and J. Q. Wu, Elastic properties of chemical-vapor-deposited monolayer MoS_2, WS_2, and their bilayer heterostructures, *Nano Lett.* 14(9), 5097 (2014)
24. V. M. Pereira and A. H. Castro Neto, Strain engineering of graphene's electronic structure, *Phys. Rev. Lett.* 103(4), 046801 (2009)
25. G. H. Ahn, M. Amani, H. Rasool, D. H. Lien, J. P. Mastandrea, J. W. III Ager, M. Dubey, D. C. Chrzan, A. M. Minor, and A. Javey, Strain-engineered growth of two-dimensional materials, *Nat. Commun.* 8(1), 608 (2017)
26. S. Deng, A. V. Sumant, and V. Berry, Strain engineering in two-dimensional nanomaterials beyond graphene, *Nano Today* 22, 14 (2018)

27. A. Castellanos-Gomez, R. Roldan, E. Cappelluti, M. Buscema, F. Guinea, H. S. J. van der Zant, and G. A. Steele, Local strain engineering in atomically thin MoS_2, *Nano Lett.* 13(11), 5361 (2013)
28. Y. Y. Hui, X. F. Liu, W. J. Jie, N. Y. Chan, J. H. Hao, Y. T. Hsu, L. J. Li, W. L. Guo, and S. P. Lau, Exceptional tunability of band energy in a compressively strained trilayer MoS_2 sheet, *ACS Nano* 7(8), 7126 (2013)
29. M. S. Kim, S. J. Yun, Y. Lee, C. Seo, G. H. Han, K. K. Kim, Y. H. Lee, and J. Kim, Biexciton emission from edges and grain boundaries of triangular WS_2 monolayers, *ACS Nano* 10(2), 2399 (2016)
30. W. S. Yun, S. W. Han, S. C. Hong, I. G. Kim, and J. D. Lee, Thickness and strain effects on electronic structures of transition metal dichalcogenides:2H-MX_2 semiconductors (M = Mo, W; X = S, Se, Te), *Phys. Rev. B* 85(3), 033305 (2012)
31. K. P. Dhakal, S. Roy, H. Jang, X. Chen, W. S. Yun, H. Kim, J. Lee, J. Kim, and J. H. Ahn, Local strain induced band gap modulation and photoluminescence enhancement of multilayer transition metal dichalcogenides, *Chem. Mater.* 29(12), 5124 (2017)
32. A. Ramasubramaniam, D. Naveh, and E. Towe, Tunable band gaps in bilayer transition-metal dichalcogenides, *Phys. Rev. B* 84(20), 205325 (2011)
33. X. Hu, P. Yasaei, J. Jokisaari, S. Ogut, A. Salehi-Khojin, and R. F. Klie, Mapping thermal expansion coefficients in freestanding 2D materials at the nanometer scale, *Phys. Rev. Lett.* 120(5), 055902 (2018)
34. L. N. Zhang, Z. M. Lu, Y. Song, L. Zhao, B. Bhatia, K. R. Bagnall, and E. N. Wang, Thermal Expansion Coefficient of monolayer molybdenum disulfide using micro-Raman spectroscopy, *Nano Lett.* 19(7), 4745 (2019)
35. L. Lei, Y. Z. Lun, F. Y. Cao, L. Meng, S. Y. Xing, J. F. Guo, H. Y. Dong, S. Z. Gu, K. Q. Xu, S. Hussain, Y. J. Li, Y. Sugawara, F. Pang, W. Ji, J. W. Hong, R. Xu, and Z. H. Cheng, Size-dependent strain-engineered nanostructures in MoS_2 monolayer investigated by atomic force microscopy, *Nanotechnology* 32(46), 465703 (2021)
36. K. Q. Xu, Y. H. Pan, S. L. Ye, L. Lei, S. Hussain, Q. M. Wang, Z. Y. Yang, X. M. Liu, W. Ji, R. Xu, and Z. H. Cheng, Shear anisotropy-driven crystallographic orientation imaging in flexible hexagonal two-dimensional atomic crystals, *Appl. Phys. Lett.* 115(6), 063101 (2019)
37. S. Hussain, R. Xu, K. Q. Xu, L. Lei, S. Y. Xing, J. F. Guo, H. Y. Dong, A. Liaqat, R. Iqbal, M. A. Iqbal, S. Z. Gu, F. Y. Cao, Y. J. Li, Y. Sugawara, F. Pang, W. Ji, L. M. Xie, S. S. Chen, and Z. H. Cheng, Toplayer-dependent crystallographic orientation imaging in the bilayer two-dimensional materials with transverse shear microscopy, *Front. Phys.* 16(5), 53504 (2021)
38. F. Pang, F. Y. Cao, L. Lei, L. Meng, S. L. Ye, S. Y. Xing, J. F. Guo, H. Y. Dong, S. Hussain, S. Z. Gu, K. Q. Xu, Y. J. Li, Y. Sugawara, W. Ji, R. Xu, and Z. H. Cheng, Strain-engineered rippling and manipulation of single-layer WS_2 by atomic force microscopy, *J. Phys. Chem. C* 125(16), 8696 (2021)
39. S. Hussain, R. Xu, K. Q. Xu, L. Lei, L. Meng, Z. Y. Zheng, S. Y. Xing, J. F. Guo, H. Y. Dong, A. Liaqat, M. A. Iqbal, Y. J. Li, Y. Sugawara, F. Pang, W. Ji, L. M. Xie, and Z. H. Cheng, Strain-induced hierarchical ripples in MoS_2 layers investigated by atomic force microscopy, *Appl. Phys. Lett.* 117(15), 153102 (2020)
40. S. Benaglia, C. A. Amo, and R. Garcia, Fast, quantitative and high resolution mapping of viscoelastic properties with bimodal AFM, *Nanoscale* 11(32), 15289 (2019)
41. Z. Y. Zheng, R. Xu, K. Q. Xu, S. L. Ye, F. Pang, L. Lei, S. Hussain, X. M. Liu, W. Ji, and Z. H. Cheng, Real-space visualization of intercalated water phases at the hydrophobic graphene interface with atomic force microscopy, *Front. Phys.* 15(2), 23601 (2020)